Ultra-fast three-dimensional X-ray imaging of deformation modes in ZnO nanocrystals

Journal:	*Nano Letters*
Manuscript ID	nl-2016-046525
Manuscript Type:	Communication
Date Submitted by the Author:	07-Nov-2016

Complete List of Authors:	Cherukara, Mathew; Argonne National Laboratory, X-ray Sciences Division Sasikumar, Kiran; Argonne National Lab Narayanan, Badri; Argonne National Laboratories, Center for Nanoscale Materials Mcnulty, Ian; Argonne National Lab Cha, Wonsuk; Argonne National Lab Wen, Haidan; Argonne National Lab Dufresne, Eric; Argonne National Lab Peterka, Tom; Argonne National Lab Sankaranarayanan, Subramanian; Argonne National Laboratory, Center for Nanoscale Materials Leake , Steven; ESRF Harder, Ross; Argonne National Laboratory,

Ultra-fast three-dimensional X-ray imaging of deformation modes in ZnO nanocrystals

Mathew J. Cherukara[1,†], Kiran Sasikumar[2,†], Wonsuk Cha[1], Badri Narayanan[2], Steven J. Leake[3], Eric M. Dufresne[1], Tom Peterka[4], Ian McNulty[2], Haidan Wen[1], Subramanian K.R.S. Sankaranarayanan[2,*], Ross J. Harder[1,*]

[1]*X-ray Science Division, Argonne National Laboratory, Argonne, IL, U.S.A*

[2]*Center for Nanoscale Materials, Argonne National Laboratory, Argonne, IL, U.S.A*

[3] *ESRF – The European Synchrotron, CS 40220, 38043 Grenoble Cedex 9, France*

[4]*Mathematics and Computer Science, Argonne National Laboratory, Argonne, IL, U.S.A*

Imaging the dynamical response of materials following ultrafast excitation can reveal energy transduction mechanisms and their dissipation pathways, as well as material stability under conditions far from equilibrium. Such dynamical behaviour is challenging to characterize, especially *operando* at nanoscopic spatiotemporal scales. In this letter, we use x-ray coherent diffractive imaging to show that ultrafast laser excitation of a ZnO nanocrystal induces a rich set of deformation dynamics including characteristic 'hard' or inhomogeneous and 'soft' or homogeneous modes at different time scales, corresponding respectively to the propagation of acoustic phonons and resonant oscillation of the crystal. By integrating the 3D nanocrystal structure obtained from the ultrafast x-ray measurements with a continuum thermo-electro-mechanical finite element model, we elucidate the deformation mechanisms following laser excitation, in particular, a torsional mode that generates a 50% greater electric potential gradient than that resulting from the flexural mode. Understanding of the time-dependence of these mechanisms on ultrafast scales has significant implications for development of new materials for nanoscale power generation.

* Corresponding authors: rharder@aps.anl.gov, ssankaranarayanan@anl.gov
† Equal contributions

Zinc oxide (ZnO) exhibits diverse and abundant configurations at nanometer to micron scales ranging from wires, belts, springs, rings, bows, and helices. ZnO has remarkable semiconducting and piezoelectric (PZ) properties, which have traditionally formed the basis for its use in electromechanically coupled sensors and transducers.[1,2] Its piezoelectric nature combined with a direct wide bandgap (3.37 eV) and large exciton binding energy (60 meV)[3] offer prospects for use in photodetectors, optical communications, photovoltaic devices, piezoelectric devices, and nanoelectromechanical systems.[4] Moreover, ZnO is biocompatible which enables its use in biomedical applications with little toxicity.[5,6]

While ZnO has emerged as a promising material for these applications, ZnO nano-structures are also being explored for use in functional devices such as nanogenerators, actuators, and sensing devices[7] where they exhibit complex longitudinal, torsional and flexural deformation modes due to surface and crystal anisotropic effects. Upon bending in, e.g. zinc oxide nanowires (NWs), the coupling of piezoelectric and semiconducting properties creates a strain field and charge separation. This effect was recently exploited to convert mechanical energy into electric power.[1,2,8] Similarly, the strong coupling between the electronic and mechanical deformation modes is receiving a lot of attention, especially in confined geometries.[9] Since the first experiments demonstrating the near-band-edge (NBE) luminescence red-shift in bending zinc oxide NWs *via* cathodoluminescence (CL),[10,11] a great deal of research has focused on understanding the origin of various mechanical deformation modes in ZnO micro/nanowires. Although numerous novel devices and applications based on ZnO wires have been realized, fundamental studies on understanding the intricate coupling between the strain fields, charge distribution and mechanical deformation modes at the nanoscale and under non-equilibrium conditions remain scarce.

We used ultrafast x-ray coherent diffractive imaging (CDI),[12–14] informed by continuum finite-element modeling (FEM) to investigate the three-dimensional (3D) evolution of the lattice strain field in a single ZnO nanocrystal following pulsed excitation with a picosecond UV laser. This pump-probe approach was used previously to study 3D lattice dynamics[15] and temporal surface melting[16] in gold nanocrystals following laser excitation. Integrating experiment-informed FEM results with the CDI

measurements yields new insight into the ultrafast thermal-electrical-mechanical dynamics of nanocrystalline ZnO that cannot be obtained by either approach alone.

Fig. 1 shows the setup for the ultra-fast CDI experiments which we performed at beamline 7-ID-C at the Advanced Photon Source (APS). ZnO nanocrystals on a SiO_2 substrate (see **methods**) were placed on a sample stage at the center of a diffractometer. A laser system (Duetto, time-bandwidth) with a repetition rate of 6.5 MHz was used to generate ~10 ps 1064 nm optical pulses. The output of the laser is frequency tripled to 355 nm for above-band-gap excitation with an incident laser flux of 1.16 mJ/cm^2. Optical pulses were syncronized to the x-ray pulses of the APS and timed electronically to arrive at the sample at specified temporal offsets from the probe x-ray pulses. . The x-ray pulses were focused by a Kirkpatrick-Baez (K-B) mirror pair to a 50 μm spot on the sample with a transverse coherence length of 10 μm, larger than individual crystals. . The APS was operated in 24 bunch mode with a temporal spacing of 153 ns between X-ray pulses, which matched the laser repetition rate. The x-ray photon energy was set to 9.0 keV using a diamond (111) monochromator.[17] Diffracted X-ray pulses were collected by an Amsterdam Scientic Instruments (ASI) Timepix detector in the (100) Bragg geometry.[18] By employing iterative phase retrieval algorithms[19,20], a complex 3D electron density $\rho(r)$ was retrieved from the data, where the phase $\phi(r)$ yielded a projection of the atomic displacement field onto the reciprocal lattice vector of the measured Bragg peak[21]. The phase of the image is related to the distortion of the lattice through the relationship $\phi(r) = \vec{Q}.\vec{u}(r)$ where $\vec{u}(r)$ is the atomic displacement and $\vec{Q}$ is the scattering vector. To perform the pump-probe experiments, the sample was excited with a laser pulse at time t_{laser}. The sample was subsequently probed with an X-ray pulse arriving at a predetermined time t_{xray}. From the 3D diffraction pattern obtained at t_{xray}, the structure and lattice displacement in the crystal were obtained. By varying the delay between the laser and X-ray pulses ($\delta t = t_{xray} - t_{laser}$), it is possible to image the time-varying structure and displacement field in the crystal.[16,22]

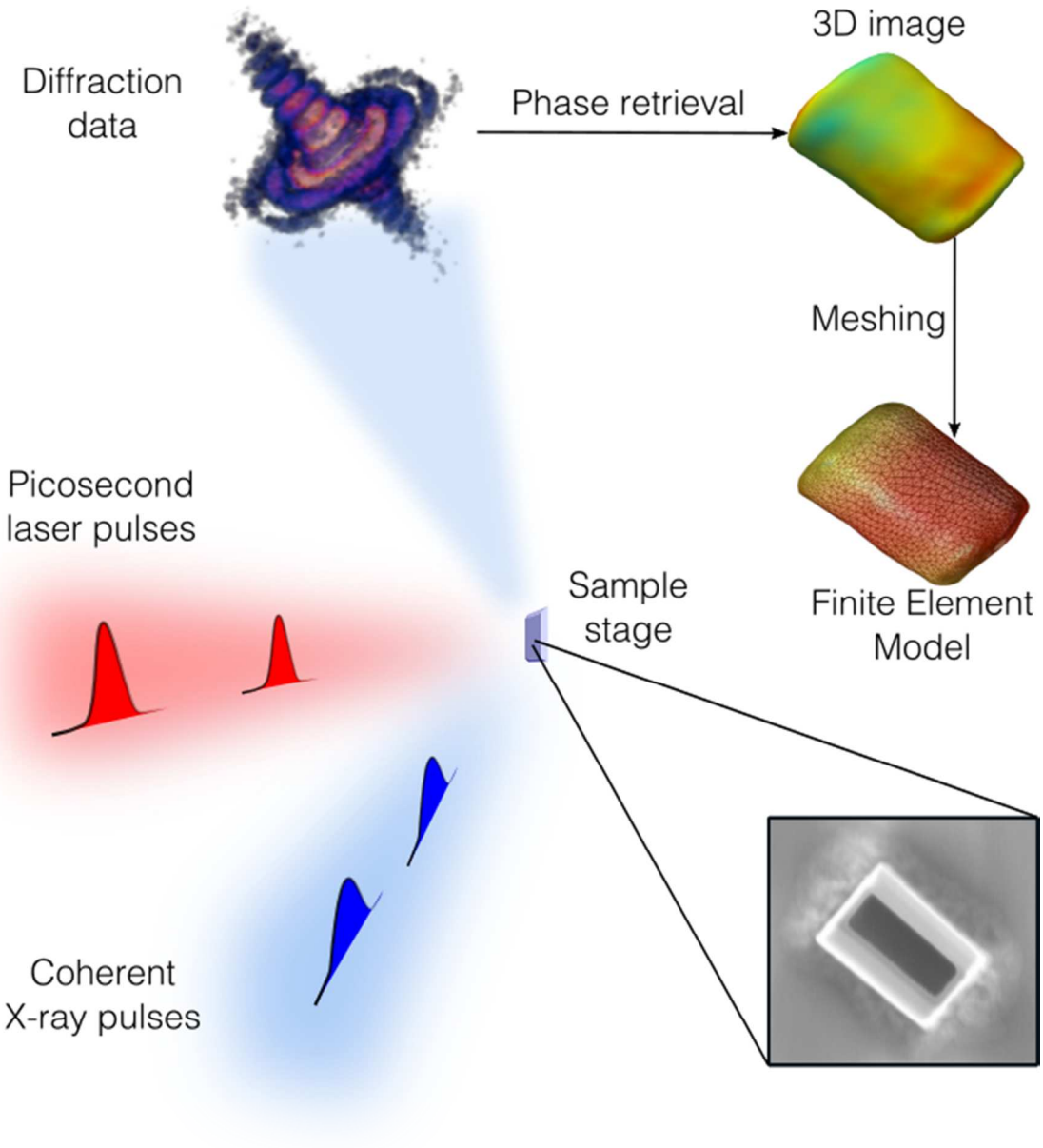

Figure 1: Ultra-fast time resolved X-ray coherent diffractive imaging. Optical pulses (red) arrive at the sample first, perturbing the ZnO nanocrystal. Coherent X-ray pulses generated from the APS (blue) arrive after a controllable delay. The diffracted X-ray pulses are recorded by an ASI Timepix detector. The crystal structure recovered from the diffraction data was imported into the continuum model.

To gain an overall picture of the dynamical response of the material, we performed continuum multi-physics simulations to complement the experimental observations. The X-ray imaged crystal structure was used as an input to the simulation model. The imported crystal volume was meshed with tetrahedral units of sizes between 1 and 50 nm, as illustrated in the Finite Element Model (FEM) shown in Fig. 1. To mimic experimental conditions, a multi-physics simulation including electrostatics, solid mechanics and heat transfer in a piezoelectric material was performed in COMSOL (see **methods**). A detailed description of the FEM simulation, the crystallographic orientations and the simulation boundary conditions is provided in the supplementary material (**see supplementary Fig. S1 and S2**).

We first analyze the various homogeneous deformation modes in the laser-excited sample. Fig. 2a-c show 2D slices through the 3D coherent diffraction pattern around the (100) Bragg peak at select delay times. Motion of the Bragg peak was observed relative to the static sample scattering vector. We denote these motions as parallel ($q_{\parallel}$) and perpendicular ($q_{\perp}$) to the static ZnO (100) Bragg condition (**Supplementary movie S1**). The peak shift along $q_{\parallel}$ can be interpreted as homogeneous strain (breathing arising from volumetric expansion and contraction) in the lattice while the peak shift along $q_{\perp}$ can be interpreted as the rotational homogeneous deformation mode of the crystal. On the other hand, the distortion in the peak is due to inhomogeneous strain in the lattice.[16] As expected, with decreasing laser fluence, both the Bragg peak shift (lattice breathing and rotation) as well as the distortion in the Bragg peak (inhomogeneous strain) becomes less pronounced (Supplementary figure S7). Fig. 2d shows the measured angular deviation of the Bragg peak as a function of delay time for a laser fluence of 1.16 mJ/cm^2, while Fig. 2e-f shows the Fourier transform of the same time signature. We observed a characteristic frequency of peak oscillation at $230 \pm 38\ MHz$ MHz for the homogeneous breathing mode. Importantly, the Bragg peak motion is also observed at negative times, where the x-ray arrives before the laser pulse. This is evidence of the crystal not returning to a rest state between the individual pump-probe pulses spaced 153 ns apart. Effectively the crystal is a driven harmonic oscillator with a primary natural frequency of ~230 MHz.

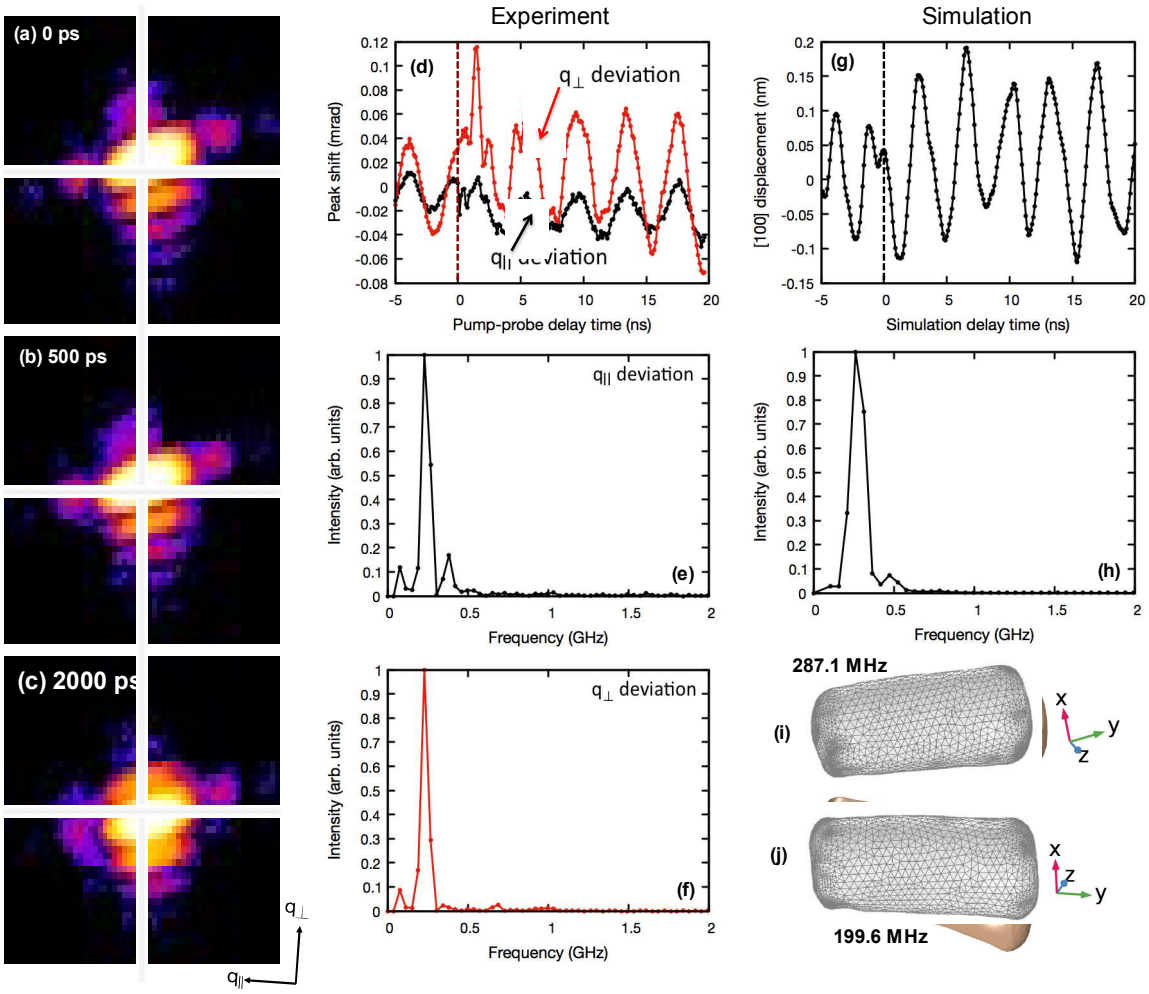

Figure 2: Time-resolved Bragg coherent diffraction data from a single ZnO crystal. Experimentally measured coherent diffraction images recorded at (a) 0 ps, (b) 500 ps and (c) 2000 ps delay from the laser. Measured intensity is depicted on a log scale. (d) Experimentally measured time-dependent shift in the Bragg peak; and (e) Fourier transform of time signal in (d) for the $q_{\parallel}$ deviations, which corresponds to the homogeneous breathing deformation mode, reveals a characteristic frequency of $230 \pm 38\ MHz$. (f) Fourier transform of time-signal in (d) for $q_{\perp}$ deviations representing the homogeneous rotational deformation mode. (g) Temporal evolution of the average crystal deformation projected along the [100] direction computed from the finite element model. This deformation corresponds to the homogeneous breathing mode. (g) Fourier transform of the time signal in (h) reveals a characteristic breathing mode frequency of $260 \pm 40\ MHz$ MHz which agrees very well with the experiments. (i)-(j) represent the dominant rotational modes and their corresponding frequencies as obtained from the eigen-mode and eigen-frequency analysis (see supporting information Fig. S3 for details).

The average displacement calculated from the FEM simulation, projected along the [100] crystallographic direction, of the ZnO crystal upon the 3rd cycle of pulsed excitation is shown in Fig. 2g. The [100] projected average displacement represents the homogeneous breathing deformation mode of the sample and is expected to correlate with $q_{\parallel}$ peak shift deviation from CDI measurements. In our simulation, the projected lattice deformation is representative of the breathing mode and oscillates with a characteristic time period of ~260 MHz (Fig. 2h), which matches reasonably well with the experiment.

To identify the homogeneous rotational deformation modes in the crystal, we perform an eigenmode analysis[23] on the simulated crystal (see supporting information Fig. S3 for details). The crystal deformation corresponding to the first two dominant rotational modes, with characteristic frequencies at ~ 290 and 200 MHz, respectively, are depicted in Fig. 2i-j. Fourier transform of time-signal in (d) for $q_{\perp}$ deviations has a dominant peak in the range $\sim 230\ MHz$, which agrees well with our eigenmode analysis. The meshed wireframe in each panel depicts the original crystal and the crystal distortion is amplified for visualization. It is worth noting that the frequency of the observed dominant deformation at ~290 MHz is consistent with an analytical solution for the flexural (rotational) mode of a hexagonal prism cantilever given by: $f_{flex} = \frac{\beta_1^2 d}{4\pi L^2}\sqrt{\frac{5E_z}{6\rho}}$ (see supplementary material for more details). The calculated value of $f_{flex} = 242\ MHz$ from the analytical solution is in agreement with experimental observation (230 +/- 38 MHz) and FEM simulations (290 +/- 40 MHz).

In addition to rotational modes, there exists faster/higher frequency inhomogeneous deformation modes that propagate axially and radially within the ZnO crystal. These so called 'hard' deformation modes are a consequence of the propagation of acoustic phonons through the crystal lattice.[15,24] Such modes cannot be identified directly by analyzing the position of the Bragg peak. Instead, we turn to the real space three-dimensional images of the displacement field in the crystal obtained from the coherent diffraction imaging to identify local variations in the strain field corresponding to these modes. Fig. 4a-c,g show the measured displacement field in 2-d slices of the ZnO nanocrystal at representative delay times following laser excitation. The measured

displacement fields show the propagation of strain waves axially (Fig 4a-c) and radially (Fig 4g). The simulated inhomogeneous deformation fields show close agreement with the experimentally observed displacement fields (Fig 4d-f,h).

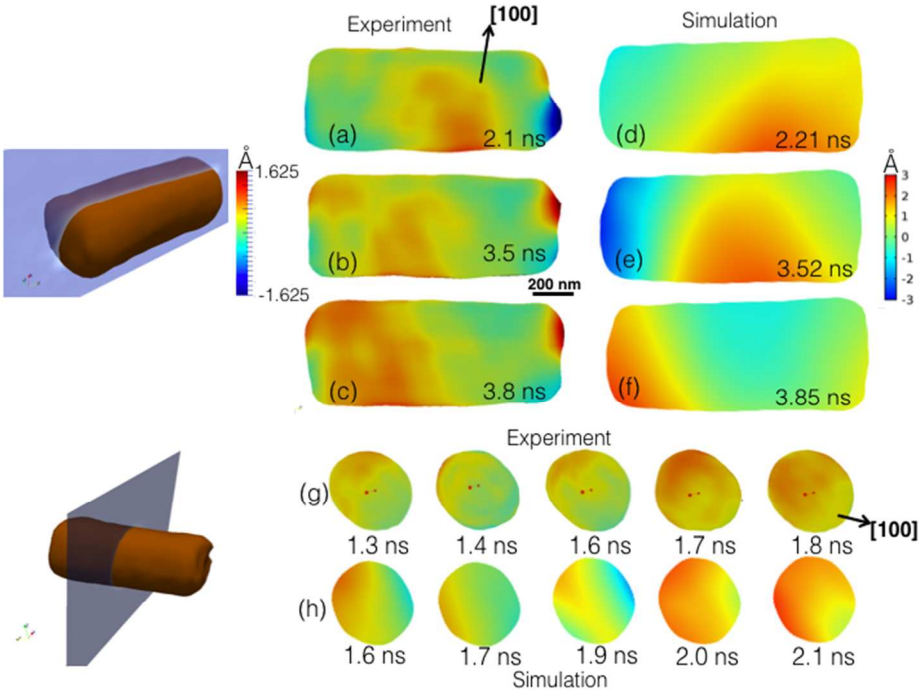

Figure 3: Time-resolved imaging of inhomogeneous deformation along the axial and radial directions in an isolated nanocrystal. (a)-(c) and (g) Cuts through the ZnO nanocrystal showing the projected displacement along the [100] direction as a function of delay time. (d)-(f) and (h) Displacement fields projected along the [100] direction as predicted by the FEM simulation.

As is evident from the axial and radial slices in Fig. 3, the time-varying deformation field shows a complex interplay between different axial (Fig. 3a-c), radial (Fig 3g) and torsional deformation modes (**see supplementary movie S2 and S3**). To better understand the nature of these various inhomogeneous deformation modes and the relative contributions of each to the observed displacement fields, we obtain a Fourier transform of the time-varying 3-D displacement field both for the experimentally measured fields as well as the simulated. This is equivalent to solving the eigenvalue problem for the deformation modes as done for Fig. 2h, (See supplementary Fig. S4). From this analysis, we obtain a 3-D representation of the local contribution to different

inhomogenous deformation modes. For instance, Fig. 4a,c show a flexural mode that results from a combination of torsion and alternating tensile-compressive waves. Black arrows describe the deformation direction. This flexural mode repeats with a frequency of ~1.5 GHz wherein the ends and the midpoints of the crystal show a maximum in lattice displacement (volume in red), while the regions in blue are relatively unperturbed. Fig4b,d describes a similar deformation mode which again is a combination of higher harmonic torsional mode and axial deformation modes. This mode has a frequency of ~2 GHz, where the lattice displacement is maximum at the ends of the nanorod (volume in red), while the bulk of the nanocrystal shows little lattice deformation (volume in blue). In good agreement with the X-ray diffraction data, our finite element simulations also shows the existence of such high frequency deformation modes that are a combination of higher harmonic torsional and axial tensile/compressive deformations as shown in Fig. 4c, d.

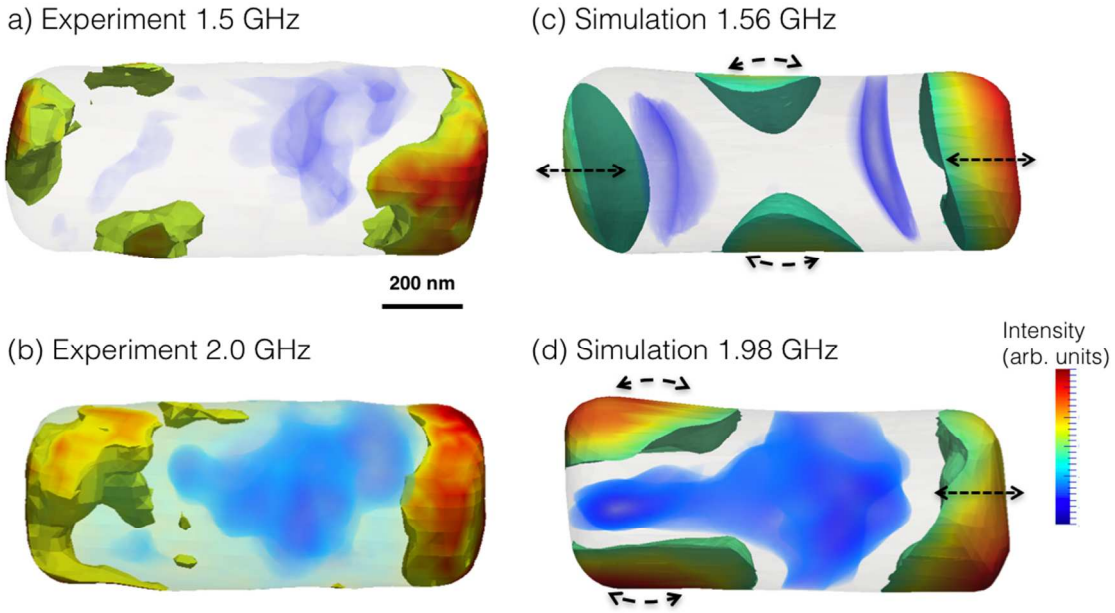

Figure 4: Imaging and simulation of the modal response of a ZnO nanocrystal. Representative high frequency deformation modes with frequency (a) 1.5 GHz and (b) 2.0 GHz imaged through CDI. Corresponding simulated deformation modes at (c) 1.56 GHz and (d)1.98 GHz are also shown. Arrows are guide to the eye to show the nature of deformation.

The implications of such higher frequency inhomogeneous deformation modes for practical applications can be significant. Recent studies have described piezoelectric energy harvesting devices that work by exploiting the homogeneous flexural deformation mode to convert mechanical energy into electrical energy.[2,25] Our experimentally informed finite element model could further be used as a predictive tool to identify other deformation modes (Fig. 5) that generate higher potential output and hence open up new opportunities for mobile/portable electronics applications. Figure 5a shows the time varying electric potential in the ZnO nanocrystal subjected to the pulsed laser excitation. The surface color maps showing electric potential distribution at representative time instants are shown in Fig. 5 b-e. These surface maps of electric potential show signatures of torsional deformation in the ZnO crystal. Fourier transform of the time-varying electric potential in Fig. 5a reveals one such dominant inhomogeneous *i.e.* torsion-like mode at ~ 2.2 GHz (Fig. 5f). This torsional mode is associated with the highest strain energy in the crystal (Fig. 5g). Fig 5h shows the crystal distortion associated with the ~2.2 GHz mode obtained from an eigenfrequency analysis in COMSOL, which correlates directly with the spatial distribution of the electric potential generated in the crystal upon pulsed laser excitation (Fig. 5b-e). Fig. 5i shows the relative electric potentials on the axial plane of the crystal of the different fundamental modes as obtained from the eigenvalue analysis. Compared to the flexural mode, the potential gradients across the ZnO crystal are seen to be 50% higher (Fig. 5j-k) for the torsion-like and higher harmonic "hard" inhomogeneous modes. A unique property of such inhomogeneous modes that have contributed to their usefulness, over the conventional flexural or bending modes, is that the torsional mode is nondispersive, *i.e.*, the propagation velocity along the medium is independent of frequency.[26,27] Torsional mode elastic transducers or piezoelectric generators and sensors that utilize the torsional mode,[28,29] along with the traditional bending modes,[1,2,8] could thus have promise in portable or mobile electronics applications.

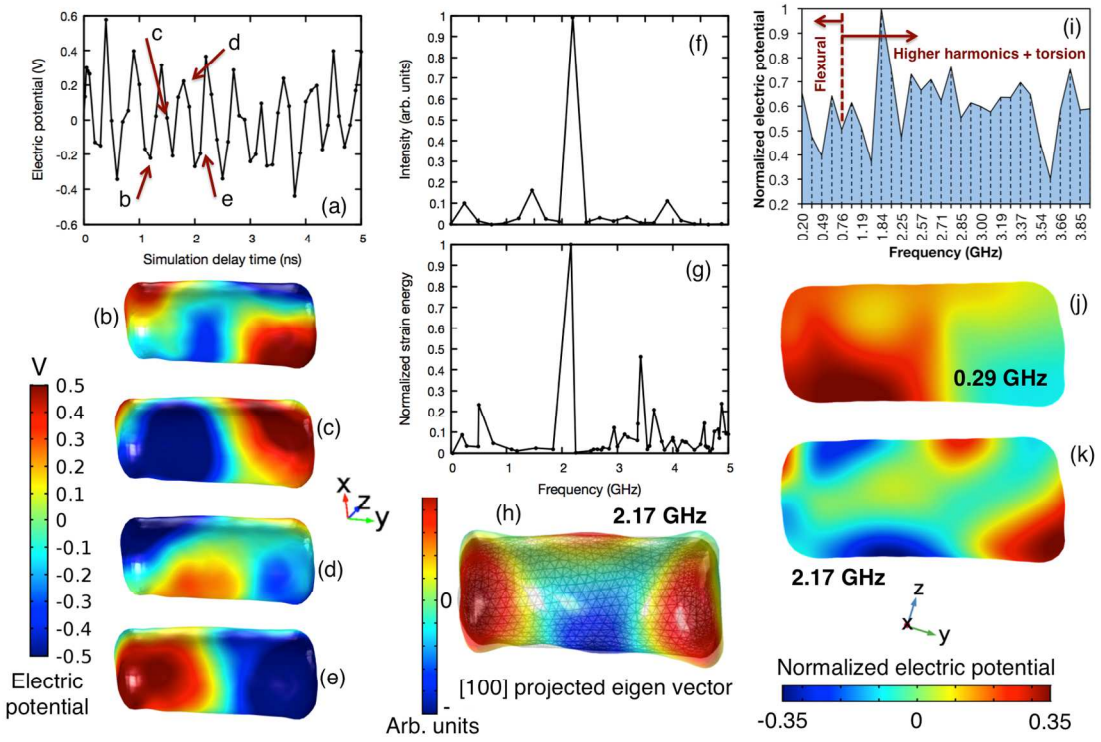

Figure 5. **Electric potential generated by the torsional deformation mode.** (a) Time-varying electric potential in the nanocrystal calculated from the FEM simulation of a pulse heated pieozelectric crystal. (b)-(e) Contour plots showing the distribution of the electric potential at the various representative time instants pointed in (a). (f) Fourier transform of the time-varying electric potential indicating that the dominant mode is ~2.2 GHz. (g) Contribution of the various deformation modes to strain energy in the crystal showing dominant mode at 2.17 GHz obtained from an eigen frequency analysis. (h) Torsional deformation mode at a frequency corresponding to the highest strain energy *i.e.* 2.17 GHz. (i) The relative electric potentials on the axial plane of the crystal of the different fundamental modes as obtained from the eigenvalue analysis. The potentials are normalized w.r.t the maximum electric potential difference, *i.e.* at the eigen frequency of 1.84 GHz. (j-k) The normalized electric potential distribution in the axial plane of the crystal for representative flexural/rotational mode (~290 MHz) and a dominant torsion mode (~2.17 GHz).

In summary, we find that ultrafast laser excitation of a ZnO nanocrystal triggers multiple homogeneous (breathing and rotational) and inhomogeneous (axial, radial, and torsional) deformation modes with different characteristic time scales. Ultrafast x-ray coherent diffractive imaging enabled three-dimensional *operando* study of these modes

on spatiotemporal scales and with a lattice strain resolution (~0.01 Å) relevant to nanoscale power generation. Integration of *experiment-informed* multi-physics simulations with the x-ray imaging data enabled identification of a torsional mode that yields an electric potential gradient across the crystal 50% higher than that resulting from the homogeneous flexural mode utilized up to now in piezoelectric based nanoscale power-generation devices. This effect could be exploited to achieve higher efficiency nanoscale power generators than existing ones that rely solely on homogeneous deformation modes. Beyond a better understanding of the dynamic behavior of materials, this powerful approach can aid in tailoring and design of mechanical, optical and piezoelectric responses of materials for the next generation of sensors, actuators and energy harvesting devices.

Methods:

Sample preparation: ZnO crystals were prepared through a modified chemical vapour deposition process where the growth occured in the gas phase and crystals are subsequently deposited on a substrate downstream. A mixture of zinc carbonate ($ZnCO_3.2Zn(OH)_3.H_2O$) and graphite powder were placed in a silica boat at the centre of a quartz tube within a Carbolite furnace maintained at 900^o C. Argon was used as the carrier gas. The decomposition of the carbonate resulted in the formation of ZnO via the reaction: $ZnCO_3 \xrightarrow{Heat} ZnO + CO_2$.

Finite Element Simulation: An exposed surface of ZnO (see Fig. S1) is heated with a 50 ps pulsed laser of 96 mW every 150 ns. The heat power is chosen to reproduce the experimental laser fluence of 1.16mJ/cm^2, such that the energy delivered to the nanocrystal over the heating cycle is the same (2.9239 nJ). The laser absorption coefficient is taken to be 0.5 in our calculations, considering the spectral emissivity of ZnO coatings at the pump laser wavelength of ~350 nm.[30]

Acknowledgements:

This work was supported by Argonne LDRD 2015-149-R1 (Integrated Imaging, Modeling, and Analysis of Ultrafast Energy Transport in Nanomaterials). Work at the

Advanced Photon and the Center for Nanoscale Materials was also supported by the U. S. Department of Energy, Office of Science, Office of Basic Energy Sciences, under Contract No. DE-AC02-06CH11357. Sample preparation was supported by EPSRC Grant No. EP/D052939/1.

References:

(1) Yang, Y.; Guo, W.; Pradel, K. C.; Zhu, G.; Zhou, Y.; Zhang, Y.; Hu, Y.; Lin, L.; Wang, Z. L.; Y. Yang, W. Guo, K. C. Pradel, G. Zhu, Y. Zhou, Y. Zhang, Y. Hu, L. Lin, Z. L. W. *Nano Lett.* **2012**, *12* (6), 2833–2838.

(2) Wang, Z. L.; Song, J. *Science (80-.).* **2006**, *312* (5771), 242–246.

(3) Teke, A.; Özgür, Ü.; Doğan, S.; Gu, X.; Morkoç, H.; Nemeth, B.; Nause, J.; Everitt, H. O. *Phys. Rev. B - Condens. Matter Mater. Phys.* **2004**, *70* (19), 1–10.

(4) Mishra, Y. K.; Modi, G.; Cretu, V.; Postica, V.; Lupan, O.; Reimer, T.; Paulowicz, I.; Hrkac, V.; Benecke, W.; Kienle, L.; Adelung, R. *ACS Appl. Mater. Interfaces* **2015**, *7* (26), 14303–14316.

(5) Zhou, J.; Xu, N.; Wang, Z. L. *Adv. Mater.* **2006**, *18* (18), 2432–2435.

(6) Dagdeviren, C.; Hwang, S. W.; Su, Y.; Kim, S.; Cheng, H.; Gur, O.; Haney, R.; Omenetto, F. G.; Huang, Y.; Rogers, J. A. *Small* **2013**, *9* (20), 3398–3404.

(7) Wang, X.; Summers, C. J.; Wang, Z. L. *Nano Lett.* **2004**, *4* (3), 423–426.

(8) Zhu, G.; Yang, R.; Wang, S.; Wang, Z. L. *Nano Lett.* **2010**, *10* (8), 3151–3155.

(9) Yang, D.-S.; Lao, C.; Zewail, A. H. *Science (80-.).* **2008**, *321* (5896), 1660–1664.

(10) Han, X.; Kou, L.; Lang, X.; Xia, J.; Wang, N.; Qin, R.; Lu, J.; Xu, J.; Liao, Z.; Zhang, X.; Shan, X.; Song, X.; Gao, J.; Guo, W.; Yu, D. *Adv. Mater.* **2009**, *21* (48), 4937–4941.

(11) Wang, Z. L. *J. Phys. Condenced Matter* **2004**, *16*, R829–R858.

(12) Chapman, H. N.; Nugent, K. A. *Nat. Photonics* **2010**, *4* (12), 833–839.

(13) Holt, M.; Harder, R.; Winarski, R.; Rose, V. *Annu. Rev. Mater. Res.* **2013**, *43* (0), 183–211.

(14) Dufresne, E. M.; Adams, B.; Chollet, M.; Harder, R.; Li, Y.; Wen, H.; Leake, S. J.; Beitra, L.; Huang, X.; Robinson, I. K. *Nucl. Instruments Methods Phys. Res. Sect.*

A Accel. Spectrometers, Detect. Assoc. Equip. **2011**, *649* (1), 191–193.

(15) Clark, J. N.; Beitra, L.; Xiong, G.; Higginbotham, A.; Fritz, D. M.; Lemke, H. T.; Zhu, D.; Chollet, M.; Williams, G. J.; Messerschmidt, M.; Abbey, B.; Harder, R. J.; Korsunsky, A. M.; Wark, J. S.; Robinson, I. K. *Science* **2013**, *341* (6141), 56–59.

(16) Clark, J. N.; Beitra, L.; Xiong, G.; Fritz, D. M.; Lemke, H. T.; Zhu, D.; Chollet, M.; Williams, G. J.; Messerschmidt, M. M.; Abbey, B.; Harder, R. J.; Korsunsky, A. M.; Wark, J. S.; Reis, D. A.; Robinson, I. K. *Proc. Natl. Acad. Sci. U. S. A.* **2015**, *112* (24), 7444–7448.

(17) Walko, D. A.; Adams, B. W.; Doumy, G.; Dufresne, E. M.; Li, Y.; March, A. M.; Sandy, A. R.; Wang, J.; Wen, H.; Zhu, Y. 2016; Vol. 30048, p 30048.

(18) Newton, M. C.; Leake, S. J.; Harder, R.; Robinson, I. K. *Nat. Mater.* **2010**, *9* (2), 120–124.

(19) Miao, J.; Sayre, D.; Chapman, H. N. *J. Opt. Soc. Am. A* **1997**, *15* (6), 1662.

(20) Fienup, J.; Wackerman, C. C. *J. Opt. Soc. Am. A* **1986**, *3* (11), 1897–1907.

(21) Robinson, I.; Harder, R. *Nat. Mater.* **2009**, *8* (4), 291–298.

(22) Robinson, I.; Clark, J.; Harder, R. *J. Opt.* **2016**, *18* (5), 54007.

(23) Tao, G.; Choubey, B. *J. Microelectromechanical Syst.* **2016**, *25* (4), 617–625.

(24) Yadav, H. K.; Gupta, V.; Sreenivas, K.; Singh, S. P.; Sundarakannan, B.; Katiyar, R. S. *Phys. Rev. Lett.* **2006**, *97* (8), 1–4.

(25) Han, X.; Kou, L.; Lang, X.; Xia, J.; Wang, N.; Qin, R.; Lu, J.; Xu, J.; Liao, Z.; Zhang, X.; Shan, X.; Song, X.; Gao, J.; Guo, W.; Yu, D. *Adv. Mater.* **2009**, *21* (48), 4937–4941.

(26) Bhaskar, A. *Proc. R. Soc. A Math. Phys. Eng. Sci.* **2003**, *459* (2029), 175–194.

(27) Thurston, R. N. *J. Sound Vib.* **1992**, *159* (3), 441–467.

(28) Pan, C. L.; Feng, Z. H.; Ma, Y. T.; Liu, Y. B. *Appl. Phys. Lett.* **2008**, *92* (1), 12923.

(29) Hoe Woong Kim; Young Eui Kwon; Joo Kyung Lee; Yoon Young Kim. *IEEE Trans. Ultrason. Ferroelectr. Freq. Control* **2013**, *60* (3), 562–572.

(30) Howell, J. R.; Menguc, M. P.; Siegel, R. *Thermal Radiation Heat Transfer, 5th Edition*; CRC Press, 2010.

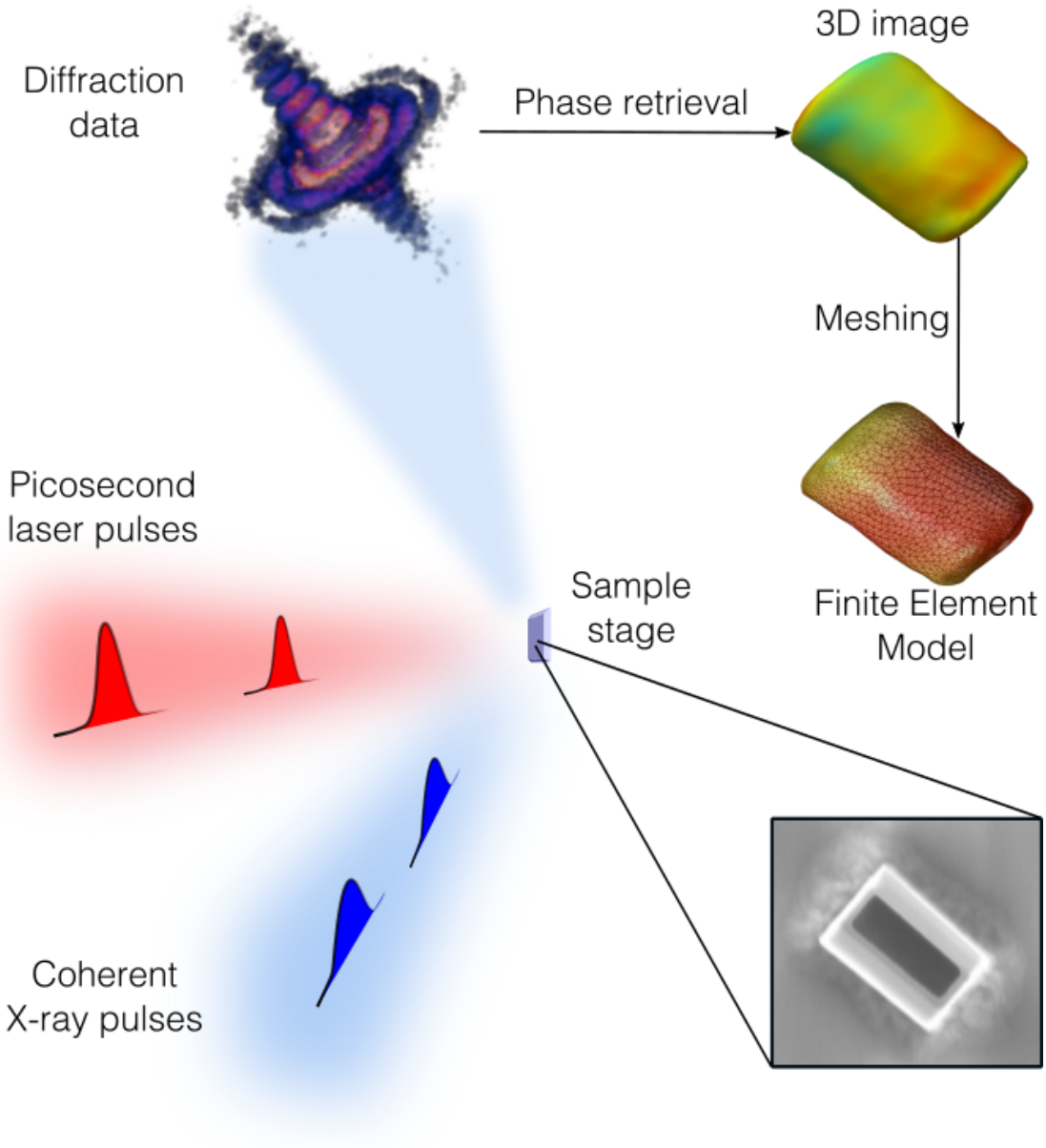
Diffraction data
Phase retrieval
3D image
Meshing
Finite Element Model
Picosecond laser pulses
Sample stage
Coherent X-ray pulses